Temperature Dependent Anomalous Mn^{2+} Emission and Excited State Dynamics in Mn^{2+}-Doped $MAPbCl_{3-x}Br_x$ Nanocrystals

BHUSHAN P. KORE,[†] SHYAMASHIS DAS,[‡] D. D. SARMA*

Solid State and Structural Chemistry Unit, Indian Institute of Science, Bengaluru-560012, India

*For Correspondence

Email: sarma@iisc.ac.in, sarma.dd@gmail.com

SYNOPSIS

Nanocrystals (NCs) of $MAPbCl_{3-x}Br_x$ doped with Mn^{2+} were prepared by simple ligand assisted reprecipitation method. Reaction temperature and Mn^{2+} concentrations were optimized to achieve maximum Mn^{2+} emission. The temperature dependent photoluminescence results reveal the origin of temperature mediated energy transfer from exciton to Mn^{2+} in $MAPbCl_{3-x}Br_x$ NCs.

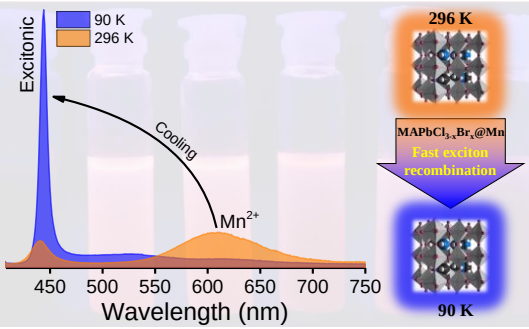

Abstract. In hybrid perovskites, $MAPbI_3$ and $MAPbBr_3$ have been extensively studied for their optical and photovoltaic properties, but $MAPbCl_3$ is significantly less investigated for its optical and photovoltaic properties due to its low photoluminescence quantum yield (PL QY) and a large band gap. However, the large band gap makes it a suitable host for doping transition metal ions to explore new optical properties. We synthesized nanocrystals (NCs) of $MAPbCl_3$ doped with Mn^{2+} by simple ligand assisted reprecipitation method. The reaction temperature and Pb to Mn feed ratio were optimized by preparing a series of Mn^{2+}-doped $MAPbCl_3$ NCs. The prepared NCs show bright Mn^{2+} emission with ~13% PL QY suggesting an efficient energy transfer from host NCs to Mn^{2+}. Since the large bandgap of $MAPbCl_3$ precludes the possibility of investigating temperature dependent PL and lifetime measurements to understand the excited state dynamics, we carried out these experiments on Mn^{2+} doped $MAPbCl_{2.7}Br_{0.3}$ with the Br concentration adjusted to bring the bandgap of the alloyed system within the limits of the experimental technique. Our studies establish an anomalous behavior of Mn^{2+} PL emission in this host. These results reveal the origin of a temperature mediated energy transfer from exciton to Mn^{2+} and provides an understanding of the underlying mechanisms of PL properties of this new class of NCs.

Keywords. Perovskite nanocrystals, anomalous photoluminescence, Mn^{2+} emission

1. Introduction

Hybrid perovskite nanocrystals (NCs) have emerged as new members of NC family with exciting optical properties.[1-4] These halide NCs have come into the spotlight due to their high quantum yields (QY), low costs and easy synthesis processes.[2,5] Colloidal $MAPbX_3$ (MA = CH_3NH_3, X = Cl, Br, or I) NCs exhibit several interesting properties, which include narrow emission bandwidths,[1] easy color tunability,[2,3] and high photoluminescence (PL) QY,[2,3,6] and high charge carrier diffusion lengths.[7] One of the most interesting and unique characteristics of these hybrid perovskites is the facile post-synthetic anion exchange among Cl, Br, and I, through which PL can be easily tuned across the entire visible spectrum.[4] Owing to these properties, the hybrid perovskite NCs have also been used in light emitting diodes (LEDs).[1,2]

Schmidt *et al.* were the first to report the colloidal synthesis of $MAPbBr_3$ NCs,[1] but the prepared NCs showed QY ca. 20% which later increased by 3 times for the NCs reported using a different synthesis route[8] and by improving the organic capping.[9] Huang *et al.* achieved PL QY as high as 93% by changing the reaction temperature within 0-60 ^oC.[10] Recently, Zhang *et al.* reported the synthesis of air stable $MAPbI_3$ NCs by investigating the interactions between perovskite precursors and various polar solvents.[11]

In hybrid perovskites, the nanocrystals of $MAPbCl_3$ are less extensively investigated compared to that of $MAPbI_3$ and $MAPbBr_3$. $MAPbCl_3$ is known to have a lower PL QY[12] in comparison with $MAPbI_3$ and $MAPbBr_3$ colloidal nanocrystals. This poor QY hinders possible applications of $MAPbCl_3$ in optoelectronic devices, in spite of the fact that the bulk $MAPbCl_3$ is known to have a better stability than the bromide and the iodide counterparts.[13] Addition of a small quantity of Cl to $MAPbI_3$/ $MAPbBr_3$ is known to improve the materials optical[14] and electrical[15-20] properties along with an improved stability.[21,22] $MAPbCl_3$ is a high band gap material,[23] which limits its application in solar cells; at the same time, its high band gap makes it a promising host material for studying the optical properties with doping of transition metal ions, such as Mn or Cu. It is well known that improved magnetic and PL properties can be obtained by doping an activator into II−VI[24-27] and III−V[25,28] NCs. In these systems, the commonly used dopants are Mn^{2+},[24,29-31] and Cu^{2+}.[29] Particularly, the optical[24,30,32-36] and magnetic[30,31,37] properties of Mn^{2+}-doped NCs have been widely explored in these semiconductors. The Mn^{2+}-doped semiconductor NCs give an intense PL at ~2.10 eV[24] owing to its forbidden $^4T_1$ to $^6A_1$ transition and it has been shown[34,36] that

this energy can be tuned over a wide range of emission wavelength by controlling the dopant site. The energy transfer from host or exciton to the Mn^{2+} activates this Mn *d-d* transition.[38] The high band gap of $MAPbCl_3$ and the possibility of Mn^{2+}-doping in modifying the optical properties of the host have motivated us to study the optical properties of $MAPbCl_3$ NCs doped with Mn^{2+}. It is curious to note that there are only a limited number of reports available[39,40,41] on the PL properties Mn^{2+} doped $MAPbCl_3$ and $MAPbCl_{3-x}Br_x$ NCs. The authors claim 75-90% doping of Mn^{2+} in place of Pb^{2+} in $MAPbCl_3$ NCs retaining the perovskite structure, where they achieved a quantum yield of ~11% and 16% for 90%[39] and 75%[40] Mn^{2+}-doping, respectively. This is contrary to the trend observed in Mn^{2+}-doped $CsPbCl_3$ NCs where both crystallinity and PL QY of NCs were found to deteriorate at Mn^{2+}-doping beyond about 27%.[42] The reduction of the Mn PL QY beyond a critical Mn concentration is also observed in other systems, such as Mn-doped group II-VI NCs.[43] Thus, these contradicting claims in ref 39 and 40 are puzzling. Since these[39,40,41] are the investigations of Mn-doped $MAPbCl_3$ so far reported in the literature, and that too with a very limited scope of a single dopant concentration and a fixed temperature, we felt it desirable to carry out a thorough temperature dependent investigation of the PL and related excited state dynamics, not probed so far, to understand this system better.

In the present study, $MAPbCl_3$ and $MAPbCl_{2.7}Br_{0.3}$ NCs with different extents of Mn^{2+}-doping have been investigated for the first time with steady-state and time resolved PL spectroscopies over a wide temperature range. The effect of Mn^{2+}-doping concentration and reaction temperature on the PL properties were also investigated.

2. Experimental

Colloidal $MAPbCl_3$:Mn^{2+} perovskite NCs were prepared by ligand-assisted re-precipitation (LARP) technique reported by Zhang *et al.*,[44] with some modifications. Two different synthesis approaches were adopted for the synthesis of $MAPbCl_3$ perovskite NCs (see supporting information). The PL QY of Mn^{2+} emission in $MAPbCl_3$:Mn^{2+} perovskite NCs synthesized by method 1 was higher compared to the PL QY obtained for $MAPbCl_3$:Mn^{2+} synthesized by method 2 for the same initial concentration of Mn^{2+}. Hence, all the samples reported in the manuscript are prepared using method 1. A series of samples were prepared using variable Pb/Mn feed ratio and different reaction temperatures.

The details of the synthesis procedure, cleaning of NCs and halide exchange are given in the supporting information. The doping concentration of Mn^{2+} ions in the $MAPbCl_3$:Mn^{2+} NCs was investigated by elemental analysis using inductively coupled plasma optical emission spectroscopy (ICP-AES). The results from ICP-AES measurements showed that for 0.5, 1, 5, 10, 20, 30, 40, 60 and 80% Mn present in the reactant with respect to Pb, the final products contained 0.2, 0.5, 1, 2, 9, 16, 22, 37 and 46% of Mn, respectively. The Mn concentration obtained from the ICP-AES measurements are used throughout the manuscript, unless otherwise mentioned.

3. Results and discussion

3.1 Structural properties of undoped and Mn-doped $MAPbCl_3$

3.1.1 X-ray diffraction

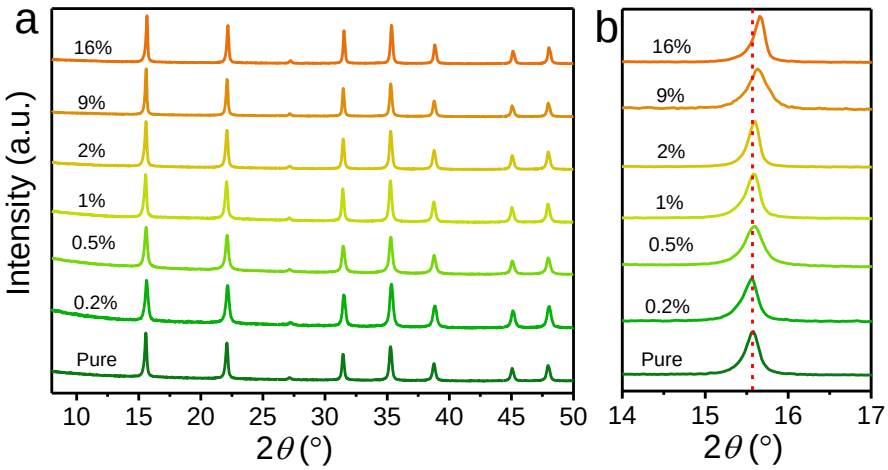

Figure 1. X-ray diffraction (XRD) patterns of (a) $MAPbCl_3$ doped with different percentage of Mn (as per elemental analysis by ICP-AES) showing preserved cubic structure for all doped concentration of Mn^{2+}, (b) a monotonic shift of the (100) XRD peak toward higher 2θ because of progressive lattice contraction with increase in doping percentage of Mn^{2+} ions.

The XRD patterns suggest that the prepared nanocrystals of pure $MAPbCl_3$ are in the cubic phase, as shown in Figure 1a. The cubic phase is retained for Mn^{2+}-doping and up to 16% of Mn doping we do not observe any impurity phase arising due to Mn or other related phases. However, for 22%, 37% and 46% Mn doping the impurity peaks were observed (see Figure S2). A careful inspection of the obtained XRD patterns reveal that the diffraction peaks shift towards higher 2θ values with an increase in Mn^{2+} content. This observed shift of 0.08° on varying Mn^{2+} concentration from 0.2 to 16% is due to the decrease in the lattice parameters with the substitution of smaller Mn^{2+} ions (0.97 Å) in place of the larger Pb^{2+} ions (1.33 Å).[45] Surprisingly, the observed

shift in the 2θ values is rather small for 16% Mn doping in view of the large size difference between the dopant Mn^{2+} and the host cation Pb^{2+}. This suggests that the lattice parameter is restricted by the large sized MA^{+} ions at the A site of the perovskite structure and also explains why this lattice cannot accommodate a larger concentration of Mn^{2+} ions following the Goldschmidt tolerance factor criterion,[46,47] giving rise to impurities at larger doping levels.

3.1.2 TEM

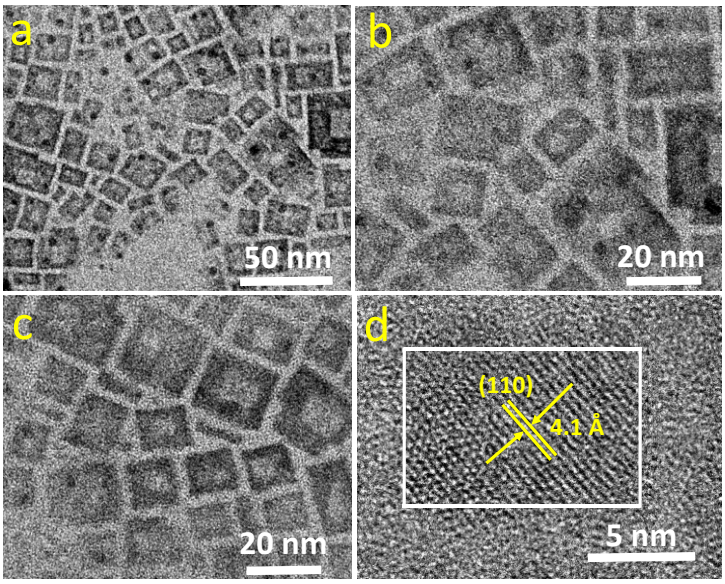

Figure 2. (a, b, c) TEM and (d) HRTEM micrographs of $MAPbCl_3:Mn^{2+}$ (16%) NCs showing preserved cubic structure. The distance between lattice planes in the HRTEM image is 3.55 Å, consistent with that expected along the (110) direction of the cubic perovskite structure.

Morphology of the prepared $MAPbCl_3$ NCs were analyzed with transmission electron microscopy (TEM), as shown in Figure 2. The undoped and Mn-doped NCs have a cubic shape with an average particle size of 15±3 nm. We noticed that the rate of injecting precursor solution into toluene decides the size of the perovskite nanocrystals, with the precipitate forming larger perovskite NCs at a higher injection rate. Therefore, in this study we have kept the injection rate at 20 µl/min, to obtain the same particle size distribution between different batches of synthesis, (see Figure S3 in supporting information). The powder XRD patterns (Figure 1a) and high-resolution transmission electron microscopy (HRTEM) (Figure 2d) with clear lattice fringes demonstrate that the synthesized NCs are highly crystalline. Optical characterizations were carried out on the cleaned NCs dispersed in toluene.

3.2 Optical properties of undoped and Mn-doped $MAPbCl_3$

3.2.1 Effect of Mn^{2+} doping on PL properties

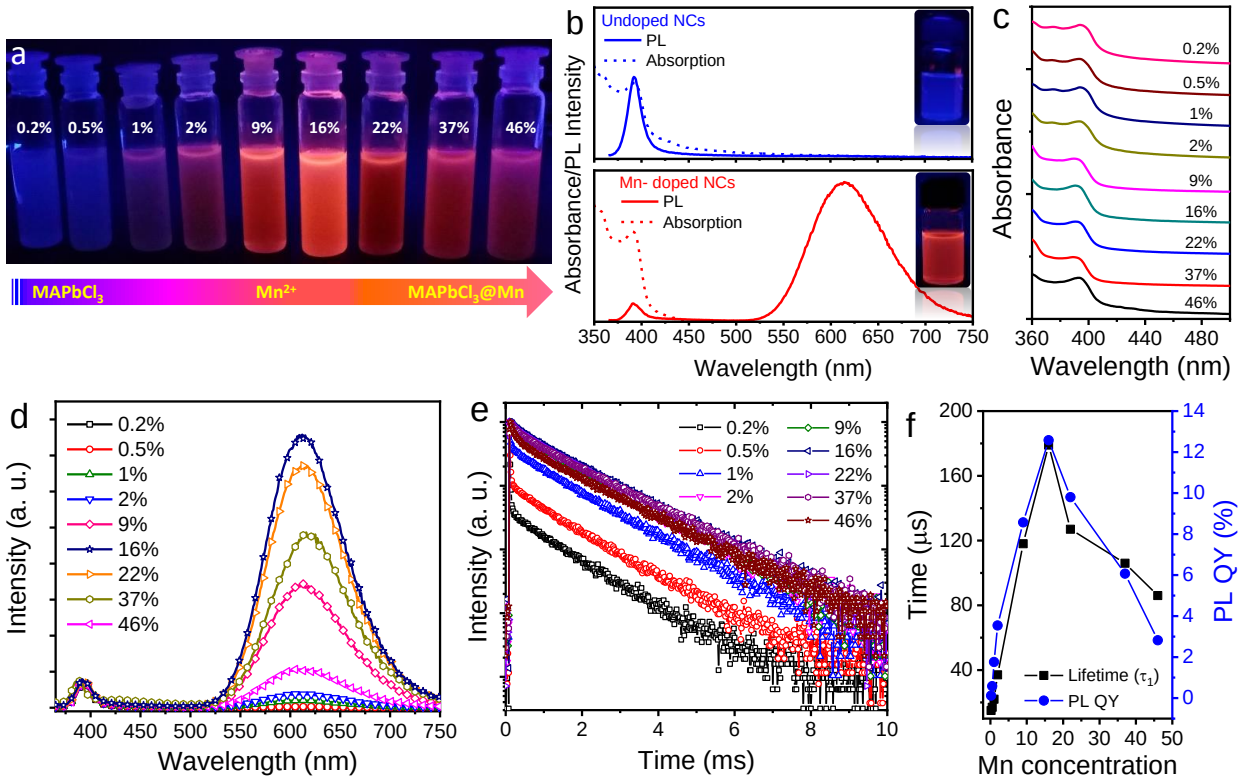

Figure 3. (a) Photograph of $MAPbCl_3$:Mn^{2+} NCs with varying the Mn^{2+}-content dispersed in toluene, illuminated under a UV lamp with ~365 nm emission wavelength. The Mn^{2+}-doped NCs show orange emission, which grows in intensity with increase in Mn concentration. (b) Absorption and PL spectra of pure and $MAPbCl_3$:Mn^{2+} (16%) perovskite NCs. The PL spectrum of Mn^{2+}-doped sample reveals a distinct emission at 615 nm corresponding to the *d-d* transition of Mn^{2+}. Insets show photographs of colloidal NCs under UV light illumination. The optical properties of $MAPbCl_3$:Mn^{2+} NCs with variation in dopant concentration. (c) Absorption and (d) PL spectra of $MAPbCl_3$:Mn^{2+} NCs with varying the Mn^{2+}-doping concentration, the PL spectra were normalized at excitonic PL. (e) Decay curves measured at the Mn^{2+} PL emission for different Mn^{2+}-doping showing a multi-exponential behavior. (f)

The effect of Mn concentration on the visible PL from Mn emission is demonstrated in Figure 3a, suggesting an optimal concentration for the brightest emission for 16% Mn-doped sample. A comparison of absorption and PL of undoped and 16% Mn^{2+}-doped $MAPbCl_3$ NCs is given in the

Figure 3b. Both the samples show almost overlapping absorption edges and excitonic PL with a full-width at half maxima (FWHM) ca. 17 nm with a peak at 392 nm. The excitonic peak in the absorption spectra of these nanocrystals appearing at 392 nm (3.16 eV) is significantly blue-shifted compared to the band gap of the bulk $MAPbCl_3$ (435 nm, 2.88 eV),[23] possibly due to the quantum confinement effects on the electronic states and the excitonic binding energies prevalent in nanomaterials.[48,49] The PL spectra of Mn^{2+}-doped sample show a broad PL emission at 615 nm (FWHM ca. 95 nm) which is due to the $^4T_{1g} - {}^6A_{1g}$ Mn^{2+} *d*–*d* transition.[24,50,53] The PL emission of Mn^{2+}-doped sample shows dominating Mn^{2+} emission compared to that of excitonic emission suggesting an efficient energy transfer from the exciton to Mn^{2+}. The insets of Figure 3b show the photographs of the weakly emitting undoped $MAPbCl_3$ NCs and strong emission in Mn^{2+}-doped NCs under UV light illumination.

As evident from the absorption spectra in Figure 3c, there is no significant shift in the band edge of the $MAPbCl_3$ NCs with a changing doping concentration of Mn^{2+}, indicating good synthesis control over the formation of $MAPbCl_3$ NCs. The absorption spectra show the presence of excitonic features in all samples. The presence of excitonic feature in the PL even at higher Mn^{2+}-doping concentrations reveals two possibilities. The first is incomplete exciton to Mn^{2+} energy transfer and second is presence of undoped $MAPbCl_3$ NCs along with the doped NCs in an ensemble of NCs. The position of the excitonic PL peak is not influenced by the Mn^{2+}-doping; only intensity of the excitonic peak gradually decrease with increase in Mn^{2+}-doping content. The PL spectra normalized at the excitonic emission, shown in Figure 3d, exhibit a systematic increase in Mn^{2+} emission up to 16% concentration of Mn^{2+} and a decrease for higher Mn contents. The decrease in the intensity can be attributed to the increase in interaction between neighboring Mn^{2+} ions at higher concentrations[43] and appearance of other impurities at higher concentrations of Mn doping. We measured the PL decay at 615 nm for all the Mn-doped samples, as shown in Figure 3e. The decay curves could be fitted well with tri-exponential decay functions in all cases with the fit parameters shown in Table S1. The multi-exponential decay curves suggest the possibility of Mn^{2+}-Mn^{2+} pair formation,[51] leading to minor fast components, though we do not see any significant redshift in the Mn^{2+} emission (see Figure S4) as observed in case of Mn^{2+}-doped $CsPbCl_3$ NCs.[51] The other possibility responsible for these faster components in the multi-exponential decay could be the migration of Mn^{2+} ions towards surface and/ or formation of trap/defect states for higher Mn^{2+}-doping.[52] We notice that the fastest component, characterized

by a_1 and τ_1 has the largest percentage for the smallest Mn^{2+} content of 0.2% (Table S1) thereafter decreasing rapidly to a relatively minor contribution of ~1-3% for Mn content ≥ 1%. Since the probability of forming interacting Mn^{2+} pairs should be expected to increase with Mn^{2+} content, it is more likely that the fastest component is primarily contributed by trap/defect states.

Table S1 makes it clear that the slowest decay (τ_3) component with a time constant in the range of 1.2-1.5 ms is the dominant contribution with about 76-88% of the decay through this channel; this is then attributed to the main Mn^{2+} radiative decay channel involving the $^4T_{1g}$ and $^6A_{1g}$ states of Mn^{2+}. The long lifetime is a consequence of this being a spin and orbitally forbidden transition, leading to a low transition probability. The Mn^{2+} lifetime initially shows a minor increase with Mn^{2+} concentration from 1.2 ms for the lowest Mn content to about 1.5 ms for 16% Mn content, remaining relatively independent of Mn concentration beyond that. The PL QY of Mn^{2+} emission shows pronounced maximum at 16% Mn^{2+} content, with the optimally doped $MAPbCl_3$ sample 100 times brighter than the PL QY (0.12%) of the excitonic emission in pure $MAPbCl_3$ NCs indicating that the energy harvesting via PL emission is made significantly more facile in presence of Mn doping for $MAPbCl_3$. In order to understand the main factor responsible for this remarkable increase in the total emission efficiency, we note that the variation of τ_1 with the Mn concentration, shown in Figure 3f, mimics exactly the change in the PL QY, suggesting τ_1 as the controlling parameter. The low PL QY of the excitonic emission for the undoped sample suggests the presence of extensive defect states providing highly efficient, lower energy pathways for non-radiative transfers of energy from the exciton to defect states in these samples. The rapid rise of Mn PL QY with Mn concentration can be interpreted in two different ways: (i) Mn doping passivates the defect states; and (ii) Mn doping provides lower energy pathways to transfer energy from the excitonic as well as defect states.[53] From our temperature dependent PL experiments, discussed later in the text, we believe that primarily the second possibility is operational in our case. τ_1, corresponding to the average time-scale of all fast processes that inhibit transfer of excited electron-hole pairs from populating the excited states of dopant Mn^{2+} ions, increases following Mn concentrations in the low doping limit due to the increasing number of available pathways to populate various Mn^{2+} centres. With an increasing Mn concentration beyond the optimal concentration of 16%, Mn-Mn dopant interactions lead to the formation of an increasing number of lower energy pathways that deplete the excitation of isolated Mn^{2+} ions, therefore once again decreasing the PL QY and τ_1.

3.2.2 Effect of reaction temperature on PL properties

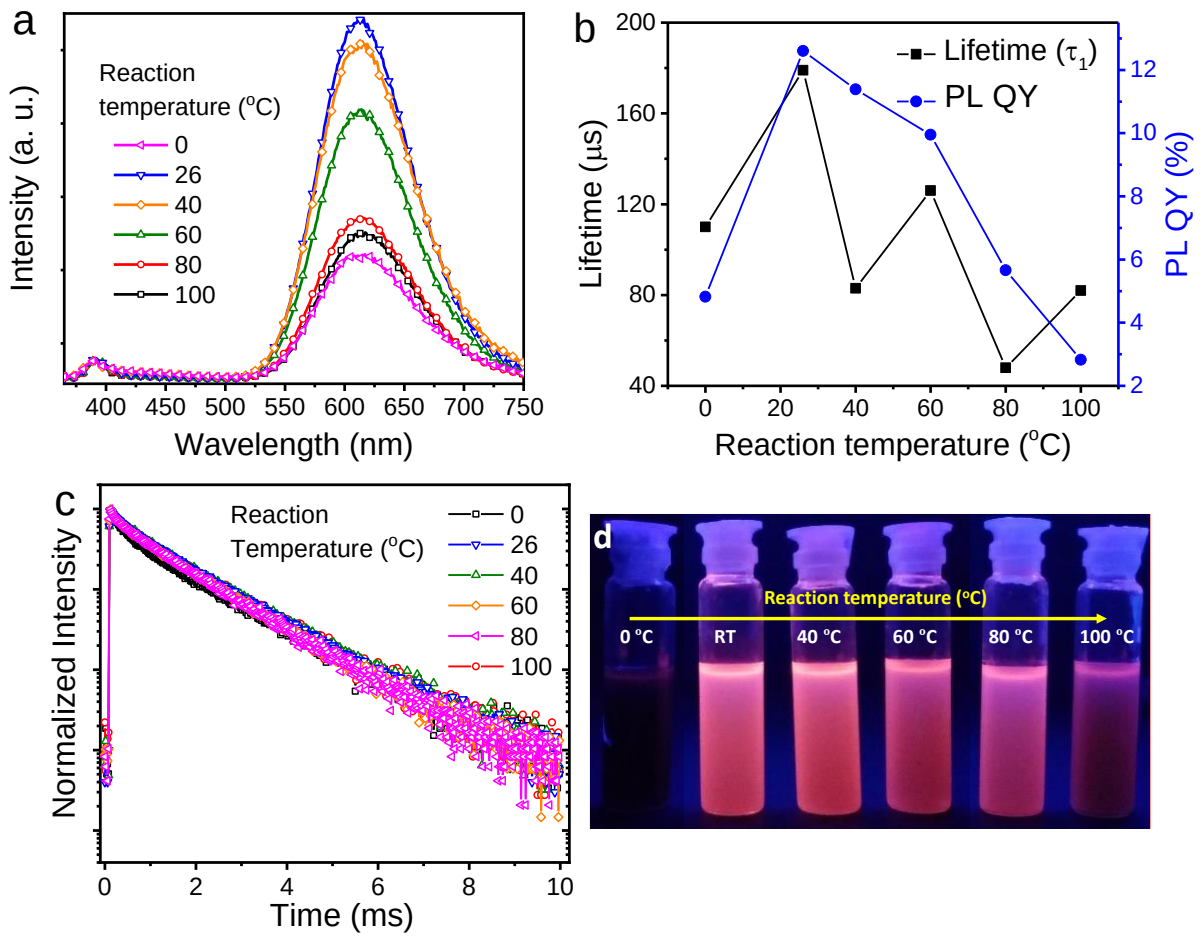

Figure 4. (a) PL spectra of $MAPbCl_3$:Mn^{2+} NCs, prepared at different reaction temperatures, normalized at excitonic PL emission. (b) Variation of Mn^{2+} lifetime (the τ_1 component) and PL QY with increase in reaction temperature. (c) Mn^{2+} emission decay curves of the $MAPbCl_3$:Mn^{2+} NCs synthesized at different reaction temperatures (plotted using cumulative offset). (d) Photograph of Mn^{2+}-doped $MAPbCl_3$ NCs dispersed in toluene with varying the reaction temperature illuminated under a UV lamp with ~365 nm emission wavelength.

To explore the effect of synthesis conditions on optical properties, a series of samples were prepared keeping the optimized Mn:Pb feed ratio constant and varying the reaction temperature (0, 26, 40, 60, 80, and 100 ºC). Figure 4a-d summarize the PL spectra and time-dependent PL intensity results. The PL spectra demonstrate that there is no significant shift in the wavelength of either excitonic emission or in Mn^{2+} emission. All the PL spectra almost overlap with each other, as shown in Figure S5; the only obvious difference is in the Mn^{2+} emission intensity, which changes rapidly depending on the reaction temperature. The maximum Mn^{2+} emission was observed for the sample prepared at room temperature, which is quantitatively established by the

PL QY results shown in Figure 4b. The decay curves of Mn^{2+} emission in the $MAPbCl_3$:Mn^{2+} NCs are shown in Figure 4c, the decay curves show a slight change in the principal lifetime of Mn^{2+} (1.31- 1.54 ms) over the variation in the reaction temperature (see Table S2). It is known that the reaction temperature influences the amount of Mn^{2+}-doping for the same Pb:Mn feed ratio.[51] Our ICP-AES results suggest a higher uptake of Mn in the samples with an increase in the reaction temperature; we observed 6%, 16%, 20%, 26%, 30%, 36% Mn content at 0, 26, 40, 60, 80, 100 ºC reaction temperature; we note here that the samples show presence of impurity peaks beyond 20% Mn^{2+} doping. Thus, we find that the variation in PL QY with the reaction temperature, shown in Figure 4b, is essentially driven by the varying Mn content, reflecting closely the variation of PL QY with Mn content shown in Figure 3d for samples synthesized at a fixed temperature, but varying the Mn content by changing the Mn concentration in the starting mixture.

The observed Mn^{2+} emission in $MAPbCl_3$:Mn^{2+} perovskite NCs is due to the energy transfer from photo-excited $MAPbCl_3$ to the doped Mn^{2+} ions. The efficiency of this process depends on how easily the host transfers the absorbed energy to the dopant. It also depends upon the internal quantum efficiency of Mn^{2+} radiative decay; the nonradiative pathways such as trap/ defect states can suppress this significantly.[51,54] While optimizing the Pb to Mn feed ratio, it was observed that the PL QY of Mn^{2+} emission increases rapidly with more Mn^{2+} substitution, which is attributed to the efficient energy transfer from exciton and defect states to Mn^{2+} with an increasing number of Mn ions available in each nanocrystal. The increase in Mn^{2+} ions increases the number of acceptor levels in the host for the photo-excited electrons and holes leading to the initial increase in the Mn PL QY. However, beyond the Mn^{2+} concentration of 16%, the PL QY drops. At such higher Mn^{2+}-doping concentrations, the decreasing distances between Mn^{2+} ions allow interactions between these dopants giving rise to non-radiative pathways, thus resulting in a decrease in the PL QY.

Our temperature dependent TCSPC spectrometer to determine the life-time of PL uses a fiber optics for coupling the spectrometer to the sample mounted in a closed cycle cryostat. Unfortunately, the optical fiber is opaque at the absorption edge of $MAPbCl_3$, making any such temperature dependent measurements impossible. To circumvent this problem, the absorption edge and the excitonic peak of the undoped and Mn^{2+} doped $MAPbCl_3$ NCs were shifted to

sufficiently higher wavelengths by halide exchange with Br, for the temperature dependent PL measurements; the details can be found in supporting information.

3.2.3 Temperature dependent PL properties of undoped $MAPbCl_{2.7}Br_{0.3}$ perovskite NCs

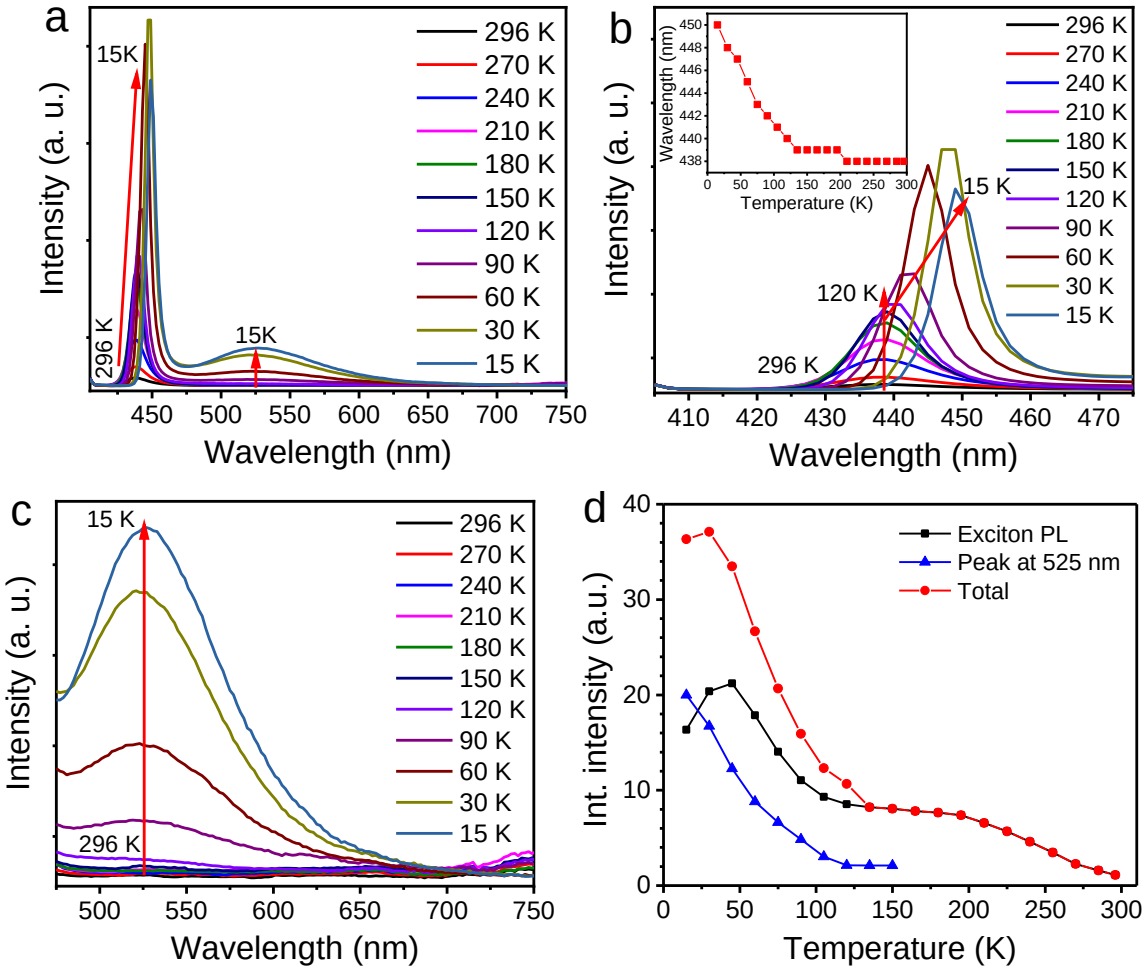

Figure 5. Temperature dependent PL spectra of undoped $MAPbCl_{2.7}Br_{0.3}$ perovskite NC film deposited on sapphire substrate, (a) over an entire temperature range excited with 400 nm. Variation of (b) excitonic PL emission and (c) 525 nm emission peak and (d) total integrated intensity with temperature. Inset in (b) shows change in excitonic peak position with variation in temperature. The temperature dependent measurements were performed in cooling mode starting from the room temperature down to 15 K, few spectra were collected in heating mode, which show a good resemblance with the data recorded in cooling mode.

To explore the energy transfer processes between the host and Mn^{2+} in more detail, temperature dependent PL and lifetime measurements were carried out. To our knowledge there has been no report on the temperature dependent PL and lifetime measurements of Mn^{2+}-doped pure or Br-alloyed $MAPbCl_{3-x}Br_x$ NCs. Figure 5a presents the steady state PL data of undoped

$MAPbCl_{2.7}Br_{0.3}$ NCs at different temperatures. The PL intensity of the excitonic emission gradually increases with lowering the temperature. The peak position of the excitonic emission remains unchanged in a high temperature cubic/tetragonal phase but below 162 K, where the system undergoes a tetragonal to orthorhombic phase transition,[55] the excitonic emission shows a pronounced and progressive red-shifting of the emission, as shown in Figure 5b. Within this low temperature phase, another PL peak emerges with a broad emission centred at about 525 nm, clearly visible in Figure 5a. A more expanded view of the same wavelength region in Figure 5c clearly shows a rapid increase in the emission intensity with a decrease in the temperature without any shift in its peak position. The sub-bandgap nature of this peak at 525 nm clearly indicates that it arises from defect states present in the NCs. The integrated intensities of the excitonic emission, defect emission and the total emission over the wavelength range shown in Figure 5a are plotted in Figure 5d as functions of the temperature. Figure 5d shows a steady rise in the total emission intensity with lowering the temperature down to about 195 K, followed by relatively temperature-independent emission intensity down to about 135 K. This is followed by a rapid rise of the total emission intensity down to 30 K and showing a signature of saturation at the lowest temperature (15 K) investigated here. By comparing with the individual emission intensities, it is clear that the T-dependency between 200 and 300 K is essentially due to the increase of the excitonic emission intensity. Such an increase in the excitonic emission intensity must be derived from the suppression of an energy transfer from the exciton to some other processes that are facile at higher temperatures. Noting that the PL QY of the emission in $MAPbCl_3$ NCs at 296 K is only about 0.12%, it is reasonable to attribute the loss of PL QY to energy transfer processes to non-radiative or low energy defect states outside the wavelength of investigation here. The decrease in the excitonic emission intensity with an increasing temperature between 200 and 300 K indicates that the energy transfer to these defect states is made facile by the increasing thermal excitation of the excitons to unbound electron and hole states, thereby reducing the excitonic emission intensity by nearly a factor of 7 over this temperature range.

Below the tetragonal-orthorhombic phase transition, the excitonic PL peak position progressively red-shifts down to the lowest temperature, indicating a continuous evolution of the underlying electronic structure, considerably more prominently than in the higher temperature tetragonal phase. Simultaneously, we also find a rapid increase in the excitonic and defect emission intensities with decreasing temperature below about 150 K. Only near the lowest temperature regime below

about 30 K, the total emission intensity shows a sign of saturation due to a compensation of the increase in the defect emission intensity by the decrease in the excitonic emission intensity.

3.2.4 Temperature dependent PL properties of Mn^{2+}-doped $MAPbCl_{2.7}Br_{0.3}$ perovskite NCs

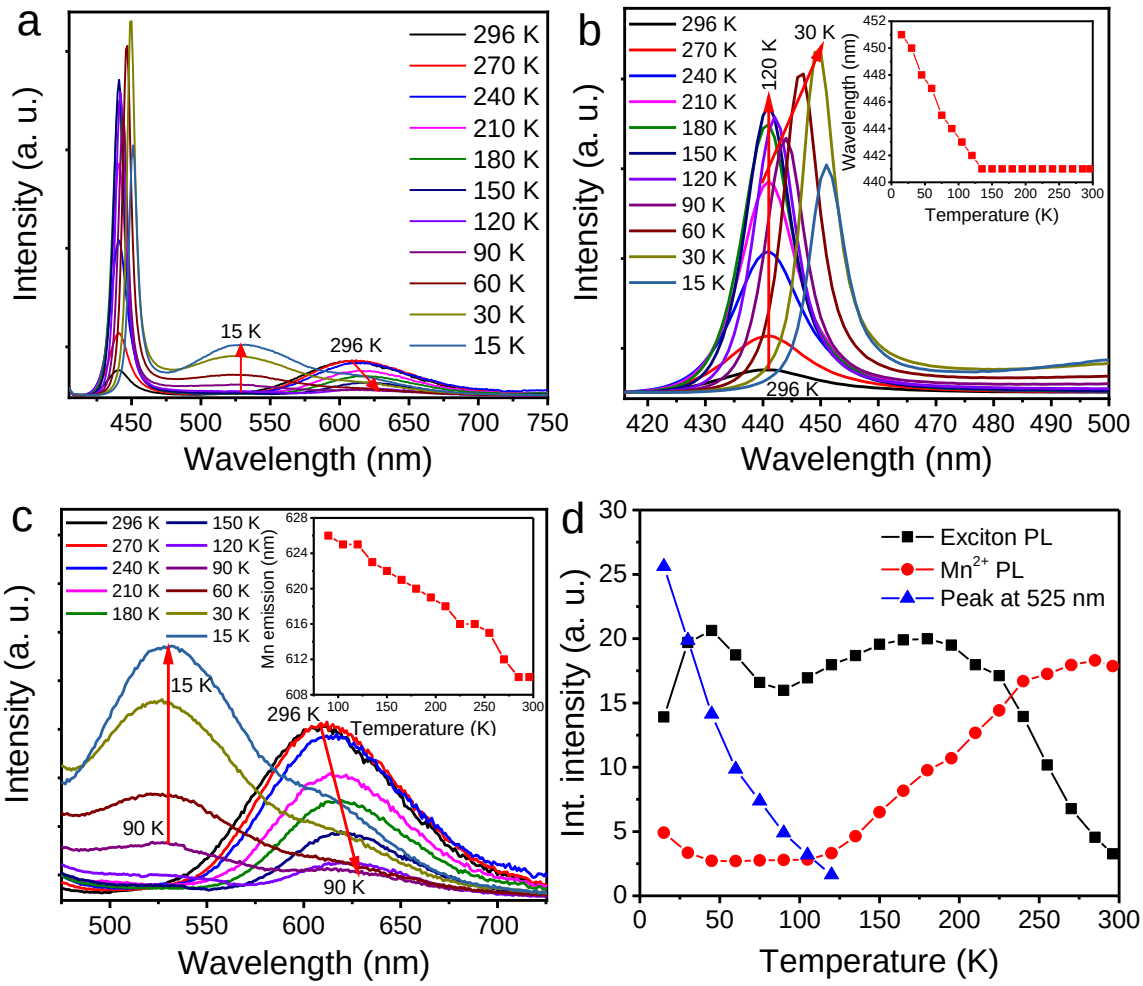

Figure 6. (a) Temperature dependent PL spectra of Mn^{2+}-doped $MAPbCl_{2.7}Br_{0.3}$ perovskite NC film, excited with 400 nm. (b) Variation of excitonic emission with lowering the temperature, the excitonic peak shows a redshift of 10 nm over the variation in temperature. (c) The change in Mn^{2+} emission and 525 nm peak with lowering the temperature. Inset of Figure c show shift in Mn^{2+} PL emission with lowering the temperature. The Mn^{2+} PL peak show significant drop in PL intensity with slightly redshifted emission at lower temperatures. (d) Integrated intensities of excitonic emission, Mn^{2+} emission and a peak at 525 nm.

The PL data of Mn^{2+} doped NCs are summarized in Figure 6 a-d in a way analogous to that in Figure 5a-d for the undoped sample. The obvious difference between the two cases, evident in panels a and c, are the appearance of the Mn^{2+} emission peak at 615 nm in Figure 6. The dependencies of the excitonic and the defect emission peaks on the temperature in the doped

sample is very similar to those of the undoped sample. Interestingly, the Mn^{2+} PL emission intensity drops drastically with lowering the temperature (see Figures 6c and d); this is a reversed trend compared to the excitonic and the defect emissions.

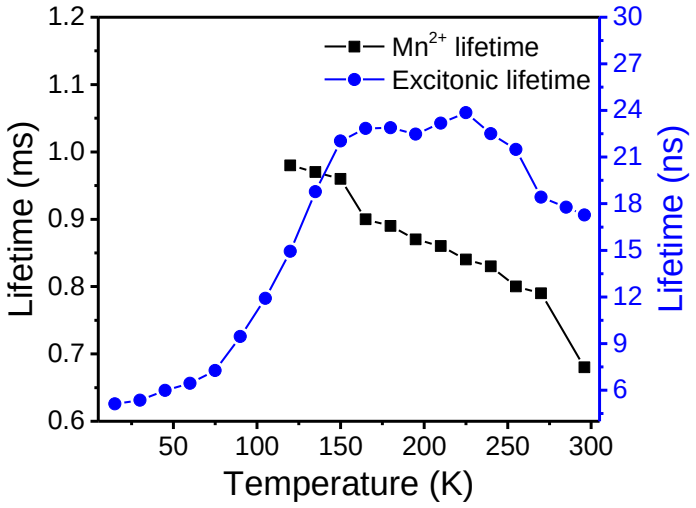

Figure 7. Calculated lifetime of excitonic emission and Mn^{2+} emission over a variation in temperature.

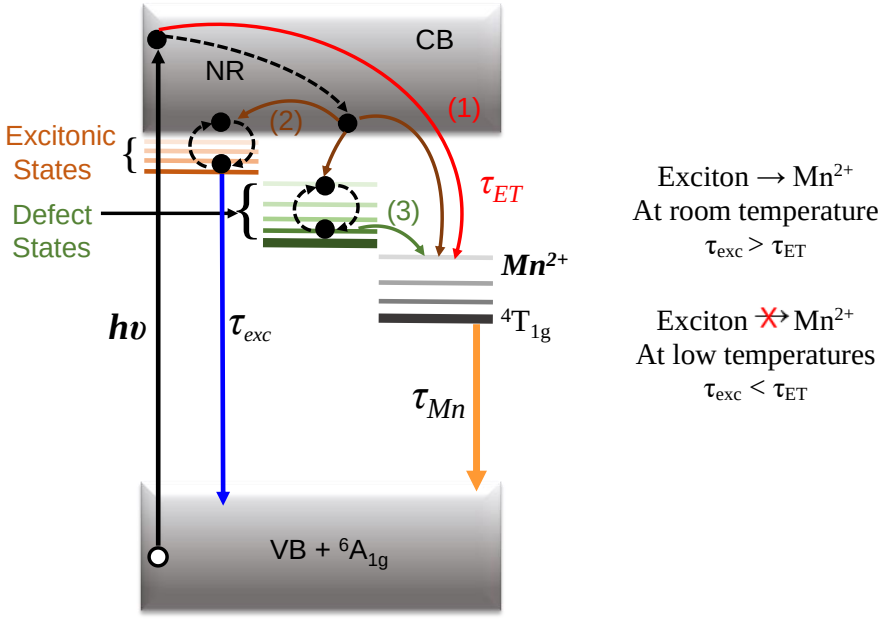

Figure 8. Schematic illustration of the energy level model to realize the energy transfer from exciton to Mn^{2+}.

This behavior of Mn^{2+} emission is also anomalous compared to the trend observed in Mn^{2+}-doped II-VI semiconductors[56-58] but nearly similar to the recent results reported for $CsPbCl_3:Mn^{2+}$.[51] A

redshift in the Mn^{2+} emission on lowering the temperature is consistent with ref. [57,59] and is attributed to the increase in crystal field strength at lower temperatures.[59]

Figure 7 summarizes the temperature dependence PL lifetime of the excitonic peak, Mn^{2+} emission. The PL lifetime as a function of temperature shows a continuous increase in Mn^{2+} decay lifetime with a lowering of the temperature. Whereas the exciton lifetime gradually decreases with lowering the temperature, which is again unusual compared to the exciton lifetime observed in II-VI NCs. In this way the PL and lifetime results obtained in the Mn^{2+}-doped $MAPbCl_{2.7}Br_{0.3}$ perovskite NCs are clearly distinct and attributed to the intrinsic property of the material.

The temperature dependent PL study reported here provides us with a plausible mechanism to understand various processes controlling unusual and anomalous optical properties of these compounds. We show the basic electronic structure that are involved in the optical transitions reported here in Figure 8. Beside the valence band (VB) of the host NC together with Mn^{2+} in its ground state $^6A_{1g}$ configuration, we have a host of excited states and pathways connecting these excited states to the ground state in these materials, as shown in Figure 8. Following the electron-hole excitation via the absorption of high energy photons, there are three distinct ways that the excited Mn^{2+} state may be populated following the high energy photoexcitation. For example, these excited electrons can either transfer their energy to Mn^{2+} (process 1) or make a transition to the lower lying states of the CB through multi-phonon relaxations. The electrons present at the bottom of the CB can also transfer their energy to the Mn^{2+} (process 2). Alternatively, the multitude of defect states present in the sample may also trap the excited electrons and/or hole as shown in Figure 8. Some of these excited defect states, lying at a higher energy, can also transfer the electrons and the hole to Mn^{2+} sites, as shown in process 3 in Figure 8. The experimental results observed here are consistent with the view that all three process (1), (2) and (3) play prominent roles in the decay mechanism. The electrons making transitions from the excitonic states to the VB gives a sharp PL peak at shorter wavelengths. However, the thermal energy at around room temperature is large enough to excite the bound state into the unbound electron and hole state, that can then be transferred to the excited Mn^{2+} state via process 2. However, with a decreasing temperature, the thermal excitation of the exciton is suppressed, leading to the observed increase of excitonic PL intensity. A similar process also influences the decay pathways involving the defect states. While it is unlikely that a defect state can be thermally excited to an electron and/or a hole in the continuum states due to the large energy difference involved, with a stokes shift of

nearly 500 meV characterizing the defect state emission, it appears clear that the thermal energy of the order of 150 K or above is enough to activate process 3. Thus, only at lower temperatures process 3 is suppressed, leading to a rapid emergence of the defect induced emission at about 525 nm. Thus, the decrease in the Mn PL emission intensity with a decrease in the temperature can be attributed to the suppression of thermal and phonon mediated processes that contribute to populating the Mn^{2+} excited states via processes 2 and 3 in Figure 8.

The decay curve analysis shows longer exciton lifetime at room temperature where Mn^{2+} has a good PL efficiency. We estimated an exciton lifetime of 18 ns from the decay curves measured at the room temperature, which is larger than the energy transfer time (τ_{ET}) of 9.3 ns from exciton to Mn^{2+}. (see supporting information) This suggests that at room temperature the excitons are decaying (τ_{exc}) slower than the τ_{ET} which gives rise to an efficient energy transfer from exciton to Mn^{2+}. The delayed lifetime of excitons at room temperatures can stem from the presence of defect states, which leads to the carrier trapping/detrapping at these states, results in longer exciton lifetime.[60,61] In some chalcogenides also, similar trend of delayed exciton emission is observed.[60,62] Therefore, at room temperature the τ_{ET} is more efficient and hence dominates. With a lowering of the temperature, the τ_{exc} gradually becomes faster. This trend makes τ_{exc} faster than the τ_{ET} below 100 K, leading to the suppression of the Mn^{2+} emission, shown in Figure 6(c) and (d). The faster decay of excitons can be evidenced from the temperature dependent exciton PL decay measurements where the exciton lifetime decreases from ~18 ns at 296 K to ~5 ns at 15 K (Figure 7). At the intermediate temperatures there is competition between the radiative decay rate of the exciton emission and τ_{ET} which determines the relative intensities of exciton and Mn^{2+} emission. The obtained energy transfer time (9.3 ns) is almost double compared to the energy transfer time reported in analogous Mn^{2+}-doped $CsPbCl_3$ perovskite NCs (3.6 ns)[63] but, much slower than reported for Mn^{2+}-doped II−VI NCs,[38,64,65] the longer τ_{ET} can be attributed to the highly ionic nature of the NCs.[66] Overall results suggest that the thermal energy (even at room temperature) is an essential physical factor which play a major role in achieving efficient exciton to Mn^{2+} energy transfer in these systems.

In temperature dependent PL, the exciton emission shows a red-shift from 441 nm to 451 nm while cooling the sample from room temperature to 15 K (Figure 6b). Generally, in most of the semiconductors a blue-shift in the exciton emission is observed upon cooling which is described

by the Varshni equation.[67] Further, from fundamental understanding point of view it is important to study the disagreement of red-shift in exciton emission present with the Varshni relation at low temperatures in these hybrid perovskites.

4. Conclusion

In conclusion, dual-emitting Mn^{2+}-doped $MAPbCl_3$ perovskite NCs have been successfully prepared by LARP method. A maximum 13% PL QY was obtained for nearly 16% Mn^{2+}-doping, which further reduced to a lower value for the higher Mn^{2+}-doping concentration confirming the formation of Mn^{2+}-Mn^{2+} pairs at higher doping. The unusual decrease in PL intensity of Mn^{2+} emission in $MAPbCl_{2.7}Br_{0.3}$ at lower temperatures reveals the importance of the temperature mediated energy transfer from exciton to Mn^{2+}. The decrease in Mn^{2+} emission intensity with lowering the temperature is a consequence of faster exciton recombination than the energy transfer to Mn^{2+} at low temperatures. The obtained results reveal the different origin of optical properties at low temperature in Mn^{2+}-doped $MAPbCl_{2.7}Br_{0.3}$ perovskite NCs than the long studied doped II-VI NCs.

Supporting Information

The supporting information includes XRD patterns, TEM micrographs, PL spectra, PL decay fitting parameters, post-synthesis halide exchange, and calculation of exciton to Mn^{2+} energy transfer time.

Acknowledgements

The authors thank Mr. Vasudeva from JNCASR for help during ICP-AES measurements. BPK acknowledges UGC, India, for a D.S. Kothari Postdoctoral Fellowship. The authors thank the Science and Engineering Research Board and the Department of Science and Technology, Government of India for support of their research. DDS thanks Jamsetji Tata Trust for support.

References

1. Schmidt, L. C.; Pertegás, A.; González-Carrero, S.; Malinkiewicz, O.; Agouram, S.; Mínguez Espallargas, G.; Bolink, H. J.; Galian, R. E.; Pérez-Prieto, J., 2014 Nontemplate Synthesis of $CH_3NH_3PbBr_3$ Perovskite Nanoparticles. *J. Am. Chem. Soc.***, 136**, 850-853.
2. Xing, J.; Yan, F.; Zhao, Y.; Chen, S.; Yu, H.; Zhang, Q.; Zeng, R.; Demir, H. V.; Sun, X.; Huan, A.; Xiong, Q., 2016 High-Efficiency Light-Emitting Diodes of Organometal Halide Perovskite Amorphous Nanoparticles. *ACS Nano***, 10**, 6623-6630.
3. Tong, Y.; Ehrat, F.; Vanderlinden, W.; Cardenas-Daw, C.; Stolarczyk, J. K.; Polavarapu, L.; Urban, A. S., Dilution-Induced Formation of Hybrid Perovskite Nanoplatelets. 2016 *ACS Nano* **10**, 10936-10944.
4. Weidman, M. C.; Seitz, M.; Stranks, S. D.; Tisdale, W. A., Highly Tunable Colloidal Perovskite Nanoplatelets through Variable Cation, Metal, and Halide Composition. 2016 *ACS Nano***, 10**, 7830-7839.
5. Mir, W. J.; Jagadeeswararao, M.; Das, S.; Nag, A., 2017 Colloidal Mn-Doped Cesium Lead Halide Perovskite Nanoplatelets. *ACS Energy Lett.*, **2**, 537-543.
6. Vybornyi, O.; Yakunin, S.; Kovalenko, M. V., 2016 Polar-solvent-free colloidal synthesis of highly luminescent alkylammonium lead halide perovskite nanocrystals. *Nanoscale***, 8**, 6278-6283.
7. Ha, S. T.; Liu, X.; Zhang, Q.; Giovanni, D.; Sum, T. C.; Xiong, Q., 2014 Synthesis of Organic–Inorganic Lead Halide Perovskite Nanoplatelets: Towards High-Performance Perovskite Solar Cells and Optoelectronic Devices. *Adv. Opt. Mater.***, 2**, 838-844.
8. Huang, S.; Li, Z.; Kong, L.; Zhu, N.; Shan, A.; Li, L., 2016 Enhancing the Stability of $CH_3NH_3PbBr_3$ Quantum Dots by Embedding in Silica Spheres Derived from Tetramethyl Orthosilicate in "Waterless" Toluene. *J. Am. Chem. Soc.***, 138**, 5749-5752.
9. Gonzalez-Carrero, S.; Galian, R. E.; Perez-Prieto, J., 2015 Maximizing the emissive properties of $CH_3NH_3PbBr_3$ perovskite nanoparticles. *J. Mater. Chem. A***, 3**, 9187-9193.
10. Huang, H.; Susha, A. S.; Kershaw, S. V.; Hung, T. F.; Rogach, A. L., 2015 Control of Emission Color of High Quantum Yield $CH_3NH_3PbBr_3$ Perovskite Quantum Dots by Precipitation Temperature. *Adv. Sci.***, 2**, 1500194-5.
11. Zhang, F.; Huang, S.; Wang, P.; Chen, X.; Zhao, S.; Dong, Y.; Zhong, H., 2017 Colloidal Synthesis of Air-Stable $CH_3NH_3PbI_3$ Quantum Dots by Gaining Chemical Insight into the Solvent Effects. *Chem. Mater.***, 29**, 3793-3799.
12. Jang, D. M.; Kim, D. H.; Park, K.; Park, J.; Lee, J. W.; Song, J. K., 2016 Ultrasound synthesis of lead halide perovskite nanocrystals. *J. Mater. Chem. C***, 4**, 10625-10629.
13. Buin, A.; Comin, R.; Xu, J.; Ip, A. H.; Sargent, E. H., 2015 Halide-Dependent Electronic Structure of Organolead Perovskite Materials. *Chem. Mater.***, 27**, 4405-4412.
14. Wehrenfennig, C.; Liu, M.; Snaith, H. J.; Johnston, M. B.; Herz, L. M., **2014** Homogeneous Emission Line Broadening in the Organo Lead Halide Perovskite $CH_3NH_3PbI_{3-x}Cl_x$. *J. Phys. Chem. Lett.***, 5**, 1300-1306.
15. Lee, M. M.; Teuscher, J.; Miyasaka, T.; Murakami, T. N.; Snaith, H. J., 2012 Efficient Hybrid Solar Cells Based on Meso-Superstructured Organometal Halide Perovskites. *Science***, 338**, 643-647.
16. Liu, M.; Johnston, M. B.; Snaith, H. J., 2013 Efficient planar heterojunction perovskite solar cells by vapour deposition. *Nature***, 501**, 395-398.
17. Du, M. H., 2014 Efficient carrier transport in halide perovskites: theoretical perspectives. *J. Mater. Chem. A***, 2**, 9091-9098.

18. Chueh, C.-C.; Liao, C.-Y.; Zuo, F.; Williams, S. T.; Liang, P.-W.; Jen, A. K. Y., 2015 The roles of alkyl halide additives in enhancing perovskite solar cell performance. *J. Mater. Chem. A*, **3**, 9058-9062.
19. Lian, Z.; Yan, Q.; Gao, T.; Ding, J.; Lv, Q.; Ning, C.; Li, Q.; Sun, J.-l., 2016 Perovskite $CH_3NH_3PbI_3(Cl)$ Single Crystals: Rapid Solution Growth, Unparalleled Crystalline Quality, and Low Trap Density toward 10^8 cm^{-3}. *J. Am. Chem. Soc.*, **138**, 9409-9412.
20. Colella, S.; Mosconi, E.; Fedeli, P.; Listorti, A.; Gazza, F.; Orlandi, F.; Ferro, P.; Besagni, T.; Rizzo, A.; Calestani, G.; Gigli, G.; De Angelis, F.; Mosca, R., 2013 $MAPbI_{3-x}Cl_x$ Mixed Halide Perovskite for Hybrid Solar Cells: The Role of Chloride as Dopant on the Transport and Structural Properties. *Chem. Mater.*, **25**, 4613-4618.
21. Cao, C.; Zhang, C.; Yang, J.; Sun, J.; Pang, S.; Wu, H.; Wu, R.; Gao, Y.; Liu, C., 2016 Iodine and Chlorine Element Evolution in $CH_3NH_3PbI_{3-x}Cl_x$ Thin Films for Highly Efficient Planar Heterojunction Perovskite Solar Cells. *Chem. Mater.*, **28**, 2742-2749.
22. Sharenko, A.; Toney, M. F., 2016 Relationships between Lead Halide Perovskite Thin-Film Fabrication, Morphology, and Performance in Solar Cells. *J. Am. Chem. Soc.*, **138**, 463-470.
23. Maculan, G.; Sheikh, A. D.; Abdelhady, A. L.; Saidaminov, M. I.; Haque, M. A.; Murali, B.; Alarousu, E.; Mohammed, O. F.; Wu, T.; Bakr, O. M., 2015 $CH_3NH_3PbCl_3$ Single Crystals: Inverse Temperature Crystallization and Visible-Blind UV-Photodetector. *J. Phys. Chem. Lett.*, **6**, 3781-3786.
24. Norris, D. J.; Yao, N.; Charnock, F. T.; Kennedy, T. A., 2001 High-Quality Manganese-Doped ZnSe Nanocrystals. *Nano Lett.*, **1**, 3-7.
25. Radovanovic, P. V.; Barrelet, C. J.; Gradečak, S.; Qian, F.; Lieber, C. M., 2005 General Synthesis of Manganese-Doped II−VI and III−V Semiconductor Nanowires. *Nano Lett.*, **5**, 1407-1411.
26. Nag, A.; Sapra, S.; Nagamani, C.; Sharma, A.; Pradhan, N.; Bhat, S. V.; Sarma, D. D., A 2007 Study of Mn^{2+} Doping in CdS Nanocrystals. *Chem. Mater.*, **19**, 3252-3259.
27. Viswanatha, R.; Naveh, D.; Chelikowsky, J. R.; Kronik, L.; Sarma, D. D., 2012 Magnetic Properties of Fe/Cu Codoped ZnO Nanocrystals. *J. Phys. Chem. Lett.*, **3**, 2009-2014.
28. Beaulac, R.; Archer, P. I.; Liu, X.; Lee, S.; Salley, G. M.; Dobrowolska, M.; Furdyna, J. K.; Gamelin, D. R., 2008 Spin-Polarizable Excitonic Luminescence in Colloidal Mn^{2+}-Doped CdSe Quantum Dots. *Nano Lett.*, **8**, 1197-1201.
29. Karan, N. S.; Sarma, D. D.; Kadam, R. M.; Pradhan, N., 2010 Doping Transition Metal (Mn or Cu) Ions in Semiconductor Nanocrystals. *J. Phys. Chem. Lett.*, **1**, 2863-2866.
30. Yu, J. H.; Liu, X.; Kweon, K. E.; Joo, J.; Park, J.; Ko, K.-T.; Lee, D. W.; Shen, S.; Tivakornsasithorn, K.; Son, J. S.; Park, J.-H.; Kim, Y.-W.; Hwang, G. S.; Dobrowolska, M.; Furdyna, J. K.; Hyeon, T., 2010 Giant Zeeman splitting in nucleation-controlled doped CdSe:Mn^{2+} quantum nanoribbons. *Nat. Mater.*, **9**, 47-53.
31. Bussian, D. A.; Crooker, S. A.; Yin, M.; Brynda, M.; Efros, A. L.; Klimov, V. I., 2009 Tunable magnetic exchange interactions in manganese-doped inverted core-shell ZnSe-CdSe nanocrystals. *Nat Mater*, **8**, 35-40.
32. Eilers, J.; Groeneveld, E.; de Mello Donegá, C.; Meijerink, A., 2012 Optical Properties of Mn-Doped ZnTe Magic Size Nanocrystals. *J. Phys. Chem. Lett.*, **3**, 1663-1667.
33. Bhargava, R. N.; Gallagher, D.; Hong, X.; Nurmikko, A., 1994 Optical properties of manganese-doped nanocrystals of ZnS. *Phys. Rev. Lett.*, **72**, 416-419.

34. Hazarika, A.; Layek, A.; De, S.; Nag, A.; Debnath, S.; Mahadevan, P.; Chowdhury, A.; Sarma, D. D., 2013 Ultranarrow and Widely Tunable Mn^{2+}-Induced Photoluminescence from Single Mn-Doped Nanocrystals of ZnS-CdS Alloys. *Phys. Rev. Lett.***, 110**, 267401.
35. Nag, A.; Sarma, D. D., 2007 White Light from Mn^{2+}-Doped CdS Nanocrystals: A New Approach. *J. Phys. Chem. C***, 111**, 13641-13644.
36. Hazarika, A.; Pandey, A.; Sarma, D. D., 2014 Rainbow Emission from an Atomic Transition in Doped Quantum Dots. *J. Phys. Chem. Lett.***, 5**, 2208-2213.
37. Cheng, S.J., 2008 Theory of magnetism in diluted magnetic semiconductor nanocrystals. *Phys. Rev. B*, **77**, 115310.
38. Chen, H.Y.; Chen, T.Y.; Son, D. H., 2010 Measurement of Energy Transfer Time in Colloidal Mn-Doped Semiconductor Nanocrystals. *J. Phys. Chem. C***, 114,** 4418-4423.
39. Arunkumar, P.; Gil, K. H.; Won, S.; Unithrattil, S.; Kim, Y. H.; Kim, H. J.; Im, W. B., 2017 Colloidal Organolead Halide Perovskite with a High Mn Solubility Limit: A Step Toward Pb-Free Luminescent Quantum Dots. *J. Phys. Chem. Lett.***, 8**, 4161-4166.
40. Li, X.; Guo, Y.; Luo, B., 2018 Improved Stability and Photoluminescence Yield of Mn^{2+}-Doped CH3NH3PbCl3 Perovskite Nanocrystals. *Crystals***, 8**, 4.
41. Min-Gi Jeon, Seokjin Yun, Artavazd Kirakosyan, Moon Ryul Sihn, Soon-Gil Yoon, and Jihoon Choi, 2019 Scale-Up Synthesis of Organometal Halide Perovskite Nanocrystals ($MAPbX_3$, X = Cl, Br, and I), ACS Sustainable Chem. Eng., **7**, 19369–19374
42. Liu, H.; Wu, Z.; Shao, J.; Yao, D.; Gao, H.; Liu, Y.; Yu, W.; Zhang, H.; Yang, B., 2017 $CsPb_xMn_{1-x}Cl_3$ Perovskite Quantum Dots with High Mn Substitution Ratio. *ACS Nano***, 11**, 2239-2247.
43. Nag, A.; Chakraborty, S.; Sarma, D. D., 2008 To Dope Mn^{2+} in a Semiconducting Nanocrystal. *J. Am. Chem. Soc.***, 130**, 10605-10611.
44. Zhang, F.; Zhong, H.; Chen, C.; Wu, X.-g.; Hu, X.; Huang, H.; Han, J.; Zou, B.; Dong, Y., 2015 Brightly Luminescent and Color-Tunable Colloidal $CH_3NH_3PbX_3$ (X = Br, I, Cl) Quantum Dots: Potential Alternatives for Display Technology. *ACS Nano***, 9**, 4533-4542.
45. Shannon, R., 1976 Revised effective ionic radii and systematic studies of interatomic distances in halides and chalcogenides. *Acta Cryst. A***, 32**, 751-767.
46. Travis, W.; Glover, E. N. K.; Bronstein, H.; Scanlon, D. O.; Palgrave, R. G., 2016 On the application of the tolerance factor to inorganic and hybrid halide perovskites: a revised system. *Chem. Sci.*, **7**, 4548-4556.
47. Kieslich, G.; Sun, S.; Cheetham, A. K., 2014 Solid-state principles applied to organic–inorganic perovskites: new tricks for an old dog. *Chem. Sci.*, **5**, 4712-4715.
48. Sameer Sapra and D. D. Sarma, 2004 Evolution of the electronic structure with size in II-VI semiconductor nanocrystals, Phys. Rev. B **69**, 125304.
49. Ranjani Viswanatha, Sameer Sapra, Tanusri Saha-Dasgupta, D. D. Sarma, 2005 Electronic structure of and quantum size effect in III-V and II-VI semiconducting nanocrystals using a realistic tight binding approach, Phys. Rev. B **72**, 045333.
50. Beaulac, R.; Archer, P. I.; van Rijssel, J.; Meijerink, A.; Gamelin, D. R., 2008 Exciton Storage by Mn^{2+} in Colloidal Mn^{2+}-Doped CdSe Quantum Dots. *Nano Lett.***, 8**, 2949-2953.
51. Yuan, X.; Ji, S.; De Siena, M. C.; Fei, L.; Zhao, Z.; Wang, Y.; Li, H.; Zhao, J.; Gamelin, D. R., 2017 Photoluminescence Temperature Dependence, Dynamics, and Quantum Efficiencies in Mn^{2+}-Doped $CsPbCl_3$ Perovskite Nanocrystals with Varied Dopant Concentration. *Chem. Mater.***, 29**, 8003-8011.

52. Xu, K.; Lin, C. C.; Xie, X.; Meijerink, A., 2017 Efficient and Stable Luminescence from Mn^{2+} in Core and Core–Isocrystalline Shell $CsPbCl_3$ Perovskite Nanocrystals. *Chem. Mater.*, **29**, 4265-4272.
53. Sapra, S.; Prakash, A.; Ghangrekar, A.; Periasamy, N.; Sarma, D. D., 2005 Emission Properties of Manganese-Doped ZnS Nanocrystals. *J. Phys. Chem. B*, **109**, 1663-1668.
54. Viswanatha, R.; Pietryga, J. M.; Klimov, V. I.; Crooker, S. A., 2011 Spin-Polarized Mn^{2+} Emission from Mn-Doped Colloidal Nanocrystals. *Phys. Rev. Lett.*, **107**, 067402-5.
55. Govinda, S.; Kore, B. P.; Swain, D.; Hossain, A.; De, C.; Guru Row, T. N.; Sarma, D., 2018 Critical Comparison of $FAPbX_3$ and $MAPbX_3$ (X= Br and Cl): How Do They Differ? *J. Phys. Chem. C*, **122**, 13758-13766.
56. Vlaskin, V. A.; Janssen, N.; van Rijssel, J.; Beaulac, R.; Gamelin, D. R., 2010 Tunable Dual Emission in Doped Semiconductor Nanocrystals. *Nano Lett.*, **10**, 3670-3674.
57. Yuan, X.; Zheng, J.; Zeng, R.; Jing, P.; Ji, W.; Zhao, J.; Yang, W.; Li, H., 2014 Thermal stability of Mn^{2+} ion luminescence in Mn-doped core-shell quantum dots. *Nanoscale*, **6**, 300-307.
58. McLaurin, E. J.; Bradshaw, L. R.; Gamelin, D. R., 2013 Dual-Emitting Nanoscale Temperature Sensors. *Chem. Mater.*, **25**, 1283-1292.
59. Chen, W.; Su, F.; Li, G.; Joly, A. G.; Malm, J.-O.; Bovin, J.-O., 2002 Temperature and pressure dependences of the Mn^{2+} and donor–acceptor emissions in ZnS:Mn^{2+} nanoparticles. *J. Appl. Phys.*, **92**, 1950-1955.
60. Rabouw, F. T.; Kamp, M.; van Dijk-Moes, R. J. A.; Gamelin, D. R.; Koenderink, A. F.; Meijerink, A.; Vanmaekelbergh, D., 2015 Delayed Exciton Emission and Its Relation to Blinking in CdSe Quantum Dots. *Nano Lett.*, **15**, 7718-7725.
61. Chirvony, V. S.; González-Carrero, S.; Suárez, I.; Galian, R. E.; Sessolo, M.; Bolink, H. J.; Martínez-Pastor, J. P.; Pérez-Prieto, J., 2017 Delayed Luminescence in Lead Halide Perovskite Nanocrystals. *J. Phys. Chem. C*, **121**, 13381-13390.
62. Cordones, A. A.; Leone, S. R., 2013 Mechanisms for charge trapping in single semiconductor nanocrystals probed by fluorescence blinking. *Chem. Soc. Rev.*, **42**, 3209-3221.
63. Parobek, D.; Roman, B. J.; Dong, Y.; Jin, H.; Lee, E.; Sheldon, M.; Son, D. H., 2016 Exciton-to-Dopant Energy Transfer in Mn-Doped Cesium Lead Halide Perovskite Nanocrystals. *Nano Lett.*, **16**, 7376-7380.
64. Chen, H.Y.; Maiti, S.; Son, D. H., 2012 Doping Location-Dependent Energy Transfer Dynamics in Mn-Doped CdS/ZnS Nanocrystals. *ACS Nano*, **6**, 583-591.
65. Chung, J. H.; Ah, C. S.; Jang, D.-J., 2001 Formation and Distinctive Decay Times of Surface- and Lattice-Bound Mn^{2+} Impurity Luminescence in ZnS Nanoparticles. *J. Phys. Chem. B*, **105**, 4128-4132.
66. Xu, K.; Meijerink, A., 2018 Tuning Exciton–Mn^{2+} Energy Transfer in Mixed Halide Perovskite Nanocrystals. *Chem. Mater.*, **30**, 5346-5352.
67. Varshni, Y. P., 1967 Temperature dependence of the energy gap in semiconductors. *Physica*, **34**, 149-154.